


Angular orientation between the cores of iron oxide nanoclusters controls their magneto-optical properties and magnetic heating functions

Enzo Bertuit¹, Nicolas Menguy², Claire Wilhelm³, Anne-Laure Rollet¹ & Ali Abou-Hassan ^{1,4}✉

Oriented attachment of nanobricks into hierarchical multi-scale structures such as inorganic nanoclusters is one of the crystallization mechanisms that has revolutionized the field of nano and materials science. Herein, we show that the mosaicity, which measures the misalignment of crystal plane orientation between the nanobricks, governs their magneto-optical properties as well as the magnetic heating functions of iron oxide nanoclusters. Thanks to high-temperature and time-resolved millifluidic, we were able to isolate and characterize (structure, properties, function) the different intermediates involved in the diverse steps of the nanocluster's formation, to propose a detailed dynamical mechanism of their formation and establish a clear correlation between changes in mosaicity at the nanoscale and their resulting physical properties. Finally, we demonstrate that their magneto-optical properties can be described using simple molecular theories.

¹Sorbonne Université, UMR CNRS 8234, PPhysico-chimie des Électrolytes et Nanosystèmes Interfaciaux (PHENIX), F-75005 Paris, France. ²Sorbonne Université, UMR 7590 CNRS—Sorbonne Université—IRD-MNHN, Institut de Minéralogie, de Physique des Matériaux et de Cosmochimie (IMPMC), Case 115, 4 Place Jussieu, 75252 Cedex 5 Paris, France. ³PSL Research University—Sorbonne Université—CNRS, UMR168, Laboratoire Physico Chimie Curie, Institut Curie, 75005 Paris, France. ⁴Institut Universitaire de France (IUF), 75231 Cedex 05 Paris, France. ✉email: ali.abou_hassan@sorbonne-universite.fr

Magnetic nanoparticles have been particularly studied during the last decades, mainly because of their interesting magnetic properties and the versatility of their surface functionalization^{1–4}. Indeed, their high saturation magnetization values and their superparamagnetic character can be used for many applications including magnetic resonance imaging⁵, sensing⁶, drug delivery⁷, for thermal therapies by magnetic hyperthermia⁸ or as more recently for their optical properties in photothermal applications^{9–11}. In the particular case of nanoclusters, the interactions between the “bricks” forming the nanoassembly can be the source of synergistic effects, making the physico-chemical properties of these objects even more particular.

In the field of materials science, the concept of colloidal molecules^{12–14}, as well as the discovery of oriented attachment mechanisms^{15–17}, have paved the way to the engineering and rationalization of a large number of structures including assemblies and clusters of different geometries and length scales^{18–22}. For example, the polyol process has shown its versatility for the preparation of many types of aggregates with controlled morphologies including iron oxide nanoclusters^{23–25}. Magnetic multi-core iron oxide nanoparticles (NPs), or nanoflowers, are quasi-monocrystalline nanostructures formed by aggregation and oriented attachment of their tiny cores. Lately, these mesocrystals have received particular attention due to their unique magnetic and optical properties especially for biomedical applications, making them one of the most efficient available nanoheaters for thermal therapies in magnetic hyperthermia and NIR-I-II photothermia^{10,24,26–28}. Although the formation of such clusters was proposed to occur through green rust intermediates^{28,29}, to date a dynamic mechanistic study on their formation correlating their structure changes with time to their physical properties in real high temperature conditions is still missing.

In this work, we explore using a multi-scale approach combining millifluidics, high-resolution transmission electron microscopy (HR-TEM), and physical characterizations (magnetic and optical) the formation of iron oxide nanoclusters with time. Insights on the mechanisms involved in nanocluster formation are elucidated thanks to millifluidics which enables a 30 s temporal resolution and an easy isolation of different formation intermediates. We show particularly how the different growth stages impact their collective magnetic and optical properties. Remarkably, we prove how little changes in the nanocluster fine structure during their growth, as reflected by mosaicity measurements, modulate their physical properties. Finally, we demonstrate that molecular theories, i.e., the magnetic exchange coupling theory for molecular magnets³⁰ and the excitonic theory³¹ for absorption of molecular H-aggregates can be extended to the level of the nanostructures to explain their magnetic and optical features.

Results and discussion

Chasing the formation of nanoflowers by time-resolved millifluidics. To understand the formation of the nanoflowers (NFs) at the nanoscale, time-resolved kinetic studies were possible due to a home-made high temperature continuous flow millifluidic device previously developed and described by our group³² (see also Supplementary Fig. 1). In addition to high chemical yields and an easy scaling up of the synthesis, this system offers an excellent temporal resolution of about 30 s. As shown in Fig. 1a, the evolution of the physical diameter (d_{TEM}) with residence times (τ_{R}) displays three distinct regimes (black, red, blue) separated respectively by characteristic exponential time constants of $\tau^1_{\text{half}} = 2.7$ min and $\tau^2_{\text{half}} = 5.9$ min. In the first phase, isolated spherical cores and small flower-like particles with approximately 5 cores of 4 nm are observed by transmission

electron microscopy (TEM) while the presence of well-defined NFs is evidenced in the second and third phases (Fig. 1b–d, see also Supplementary Figs. 2–4). The $d_{\text{TEM}} = f(\tau_{\text{R}})$ curve progression suggests that those three steps are separated by two different activation energy barriers corresponding to the transformation of flower-like structures into well-defined NFs and after of small NFs into bigger ones, respectively. To gain more insights into the NFs formation mechanism, the size of magnetic cores (d_{m}) and the number of cores (N_{MC}) per flower-like assembly are determined by VSM (see also Supplementary Fig. 5) for residence times corresponding to the second and third steps (i.e., between 3 min and 16 min, Fig. 1e). Again, two different behaviors are evidenced with a characteristic switch time of $\tau_{\text{switch}} = 6.2$ min, very close to the characteristic time of $\tau^1_{\text{half}} = 5.9$ min determined previously. Firstly, the magnetic core size increases from 4 nm to 8 nm while the number of cores remains constant around $N_{\text{MC}} = 35$. The linear evolution observed in the first step also suggests that nuclei formed at early times are about 1.7 nm in diameter. Then, the magnetic core size reaches a plateau for a value of $d_{\text{m}} = 8.3$ nm, while the number of cores increases exponentially from approximately $N_{\text{MC}} = 45$ to $N_{\text{MC}} = 75$. In a consistent way, TEM observations show an increase in the NFs diameter. Taken together, these results evidence the presence of a nucleation step before 3 min, followed by a growth step between 3 and 6 min with a final aggregation step for residence times higher than 6 min. To explore the aggregation mechanism into bigger NFs, SAXS was performed on the crude final products in polyol solvents collected at the output of the millifluidic system for each residence time (see Supplementary Fig. 6). A characteristic NF-NF interaction peak is evidenced and corresponds to a NF-NF distance similar to the NFs diameter obtained from TEM. Interestingly, no significant peak is observed in the q -range of core sizes (4–8 nm) indicating that no or undetectable isolated cores are present in the crude products. Therefore, the increase in the number of magnetic cores observed in the last stage of NFs formation can be explained by the attachment of NFs to neighbor NFs giving rise to a higher number of cores with a constant size of 8 nm. According to TEM, VSM and SAXS data, we propose the following mechanism for NFs formation (Fig. 1f). At early residence times, 1.7 nm spherical nuclei are formed (as extrapolated on $d_{\text{m}} = f(\tau_{\text{R}})$ curve) from molecular precursors reaching a final size of 4 nm. At about $\tau_{\text{R}} = 3$ min, primary poorly-defined flower-like structures composed of 5 cores of 4 nm are next formed followed by a very fast attachment of isolated cores to create 35-cores structures. Afterward, the number of cores remains constant ($3 \leq \tau_{\text{R}} \leq 6$ min) and the dissolution of molecular precursors into the nanostructures enables the growth of each core from 4 nm to 8 nm. Finally, when the core size reaches the critical value of about 8 nm, core growth stops and NFs start to attach to other NFs, yielding bigger NFs with a higher number of 8 nm cores ($\tau_{\text{R}} \geq 6$ min). By analogy with molecular magnets, this mechanistic study suggests that superparamagnetic flower-like nanoclusters may be considered as colloidal molecules formed by the assembly of several cores acting as magnetic atom centers. From now on, as we have shown that the syntheses in the millifluidic device are highly reproducible (very small error bars in Fig. 1a), we will assume that all the measured properties should be reproducible because both magnetic and optical properties strongly depend on the size and composition of the nanoparticles.

Magneto-optical properties are time-dependent. The next logical step is to investigate how these nanostructural transformations translate into changes in the NFs physical features, mainly their magnetic and optical properties (Fig. 2). Regarding magnetism, the saturation magnetization (M_{S}) of the NFs is

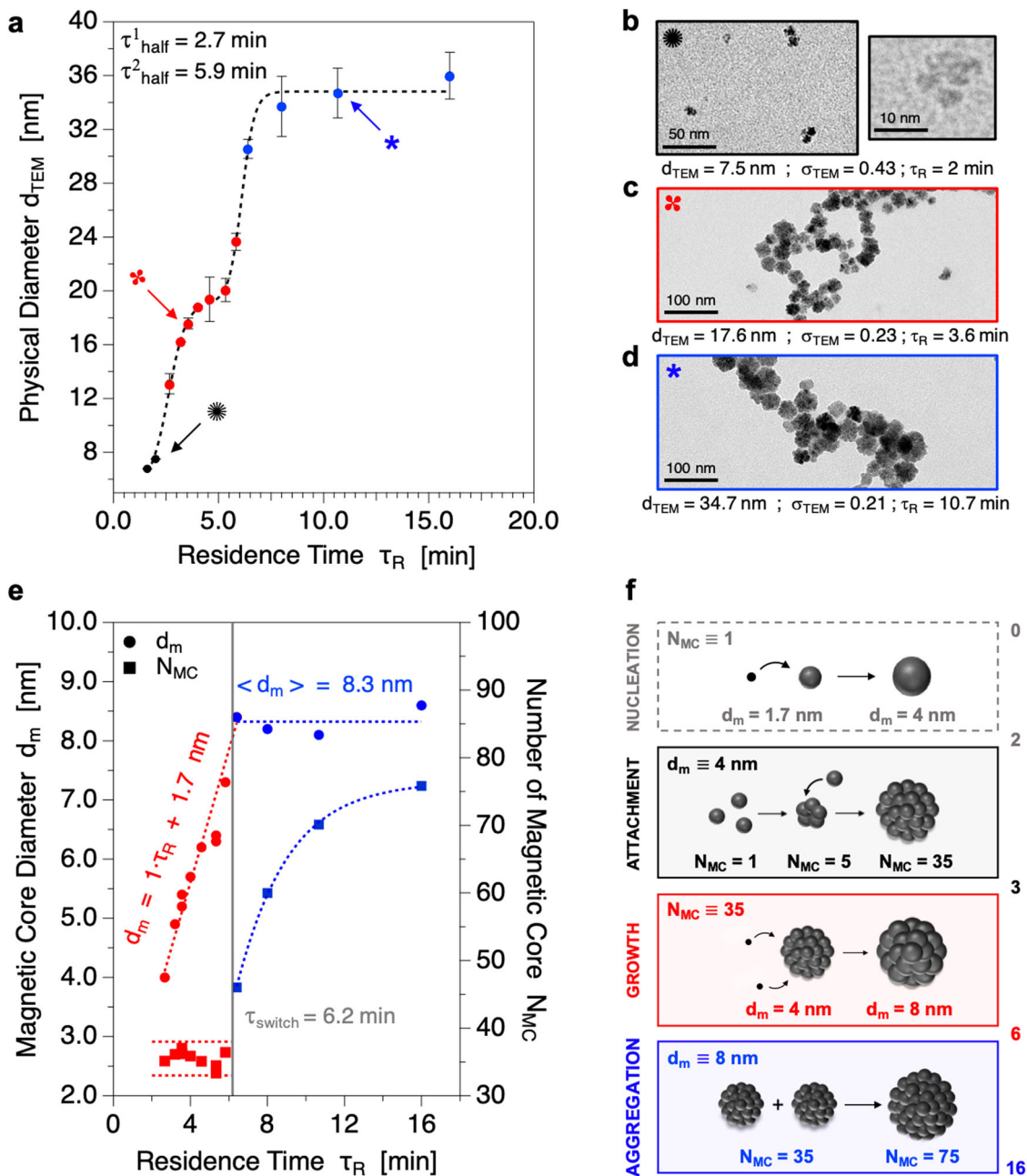


Fig. 1 Nanoscale investigation of the mechanisms involved in NFs formation. **a** Evolution of the physical diameter observed by TEM with the residence time in the system (error bars correspond to the standard deviations on diameters for 2 or 3 repeated syntheses). The residence time inside the millifluidic channel was calculated by $\tau_R = Q/V$ with Q is the total flow rate and V the total volume of the channel. **b–d** Representative TEM micrographs of 3 samples obtained respectively for residence times of 2.0, 3.6, and 10.7 min, indicated by arrows in **(a)**. **e** Evolution of the core diameter and the number of magnetic cores within the NFs assemblies with the residence time. **f** Schematic representation of the mechanisms leading to NFs morphological sequential evolutions (small black dots: iron(II) and/or iron(III) molecular precursors, dark gray balls: iron oxide cores).

found to increase with their physical diameter to reach values up to 90–95 emu/g (Fig. 2a, see also Supplementary Fig. 7) during the final aggregation stage, in good agreement with previously reported values for iron oxide NFs³³. Surprisingly, the saturation magnetization depends linearly on the size of the magnetic cores (Fig. 2b) and not on the volume of the NFs. However, it is well established that M_S increases with exchange couplings and therefore with the alignment between the crystalline planes of the different cores in the mesocrystal^{34,35}. Thus, such a result strongly suggests a progressive orientation of the magnetic cores during their growth. Besides, M_S increases with N_{MC} following two distinct rates (Fig. 2c). Firstly, during the growth stage where the

number of magnetic cores is constant ($N_{\text{MC}} \equiv 35$) and d_m grows from 4 nm to 8 nm, an increase independent from N_{MC} is observed. Then, a lower slope of about $0.3 \text{ emu} \cdot \text{g}^{-1} \cdot \text{core}^{-1}$ is evidenced when N_{MC} increases up to 75 with a constant magnetic core size of 8 nm. Interestingly, the switch from one rate to the other matches perfectly with the switch time highlighted by TEM ($\tau_R = 5.8$ min) and can be explained by the appearance of more dipolar effects that tend to decrease the rise of M_S values when N_{MC} increases, as predicted by numerical simulations³⁶. Taken together, these results suggest that the magnetic macrospin of the NFs does not result in the simple sum of each core magnetic spin but is a more complex function of both the core size and core number. The variation of

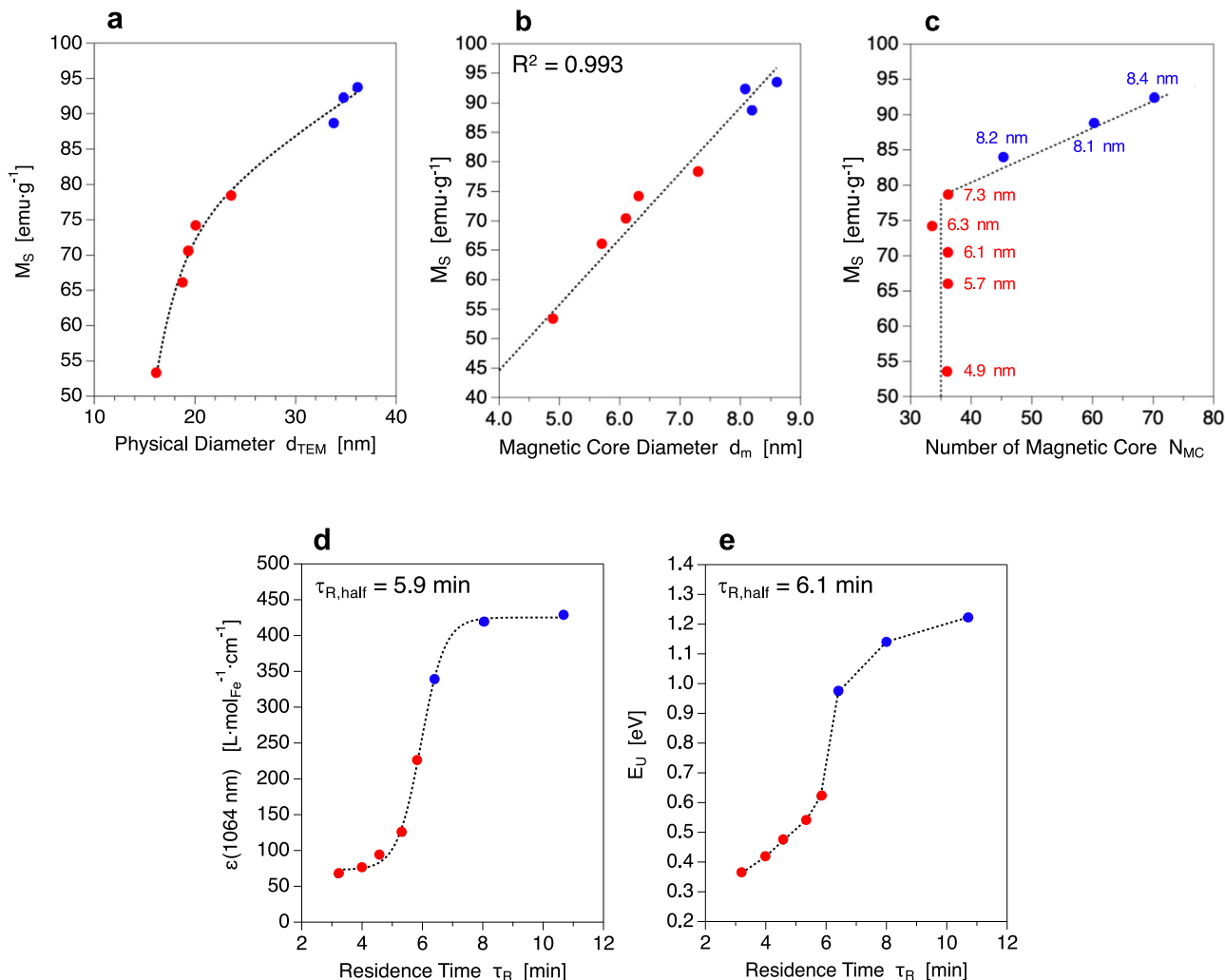


Fig. 2 Evolution of NFs static magnetic properties and optical characteristics with nanostructural features and residence time. **a–c** Saturation magnetization dependency on the physical diameter, magnetic core diameter and number of magnetic cores, respectively. **d, e** Evolution of the extinction coefficient and Urbach energy with residence time, respectively. Please note that the sizes on Fig. 2c correspond to the magnetic core diameters.

NFs electronic band structure during their formation is tracked by studying their optical properties. XANES at Fe K-edge analyses^{37–39} (see Supplementary Fig. 8) show that all samples have the stoichiometry of pure magnetite ($R = \text{Fe}^{\text{II}}/\text{Fe}^{\text{III}} = 0.5$) with an average value of $\langle R \rangle = 0.48 \pm 0.01$. Consequently, the intervalence charge transfer (IVCT)⁴⁰ between Fe^{3+} and Fe^{2+} laying in the NIR-II window is used as a fingerprint of electronic effects. The extinction coefficient in the NIR-II region (ϵ_{1064}) is deduced from UV-Vis-NIR absorption spectra (see Supplementary Figs. 9 and 10) and is found to follow a sigmoid function of residence time, again with a characteristic time $\tau_{R,\text{half}} = 5.9$ min (Fig. 2d). As ϵ_{1064} variations cannot be ascribed to differences in stoichiometry, the band structure of the semi-conductor NFs is explored and characterized by direct band-gap energy (E_g^{dir}) and defect-characteristic^{41,42} Urbach energy (E_U). Consistently with previously reported values⁴³, the same direct band-gap energy is found for all NFs with an average value of $\langle E_g^{\text{dir}} \rangle = 3.7 \pm 0.1$ eV (see Supplementary Fig. 11). The Urbach energy, which translates and quantifies the presence of all type of defects (chemical composition, structural/crystalline disorders) in semi-conductors, is then calculated from UV-Vis-NIR absorption spectra (see Supplementary Fig. 12) according to Urbach theory⁴⁴. A comparable sigmoidal evolution of E_U values with residence time is observed when compared to ϵ_{1064} variations with a similar characteristic time of $\tau_{R,\text{half}} = 6.1$ min (Fig. 2e). As E_U is inversely proportional to the number of defects,

these results strongly suggest that the increase in ϵ_{1064} is due to a diminution of defect concentration within the band structure of the NFs.

Evolution of magnetic spin relaxation processes with time. To better understand how the core transformations impact the magnetic properties of the whole NFs assemblies, dynamic magnetic properties of the NFs are next investigated. In the case of nanoclusters, it is established that magnetic interactions between each “brick” of the cluster strongly impact their resulting efficiency in magnetic hyperthermia (MHT)²⁷. For iron oxide NF-like nanoclusters, the presence of exchange couplings between the magnetic cores highly enhances the specific loss power (SLP) when compared to single-core structures such as nanospheres^{25,26} or nanocubes^{45–47}. Figure 3 shows MHT performances of the NFs under different alternative magnetic field (AMF) excitations which remain below the Atkinson-Brezovich safety limit (see also Supplementary Fig. 13)⁴⁸. For a given AMF frequency and amplitude, SLP increases with the number of magnetic cores composing the NFs rather than with the physical diameter of the assembly (Fig. 3a). When comparing the results for NFs synthesized in the microfluidic device (circles) with those obtained for round-flask NFs syntheses (squares, Bertuit et al.¹⁰), it is found that the SLP of iron oxide NFs is proportional to N_{MC} for a given AMF. Such a linear

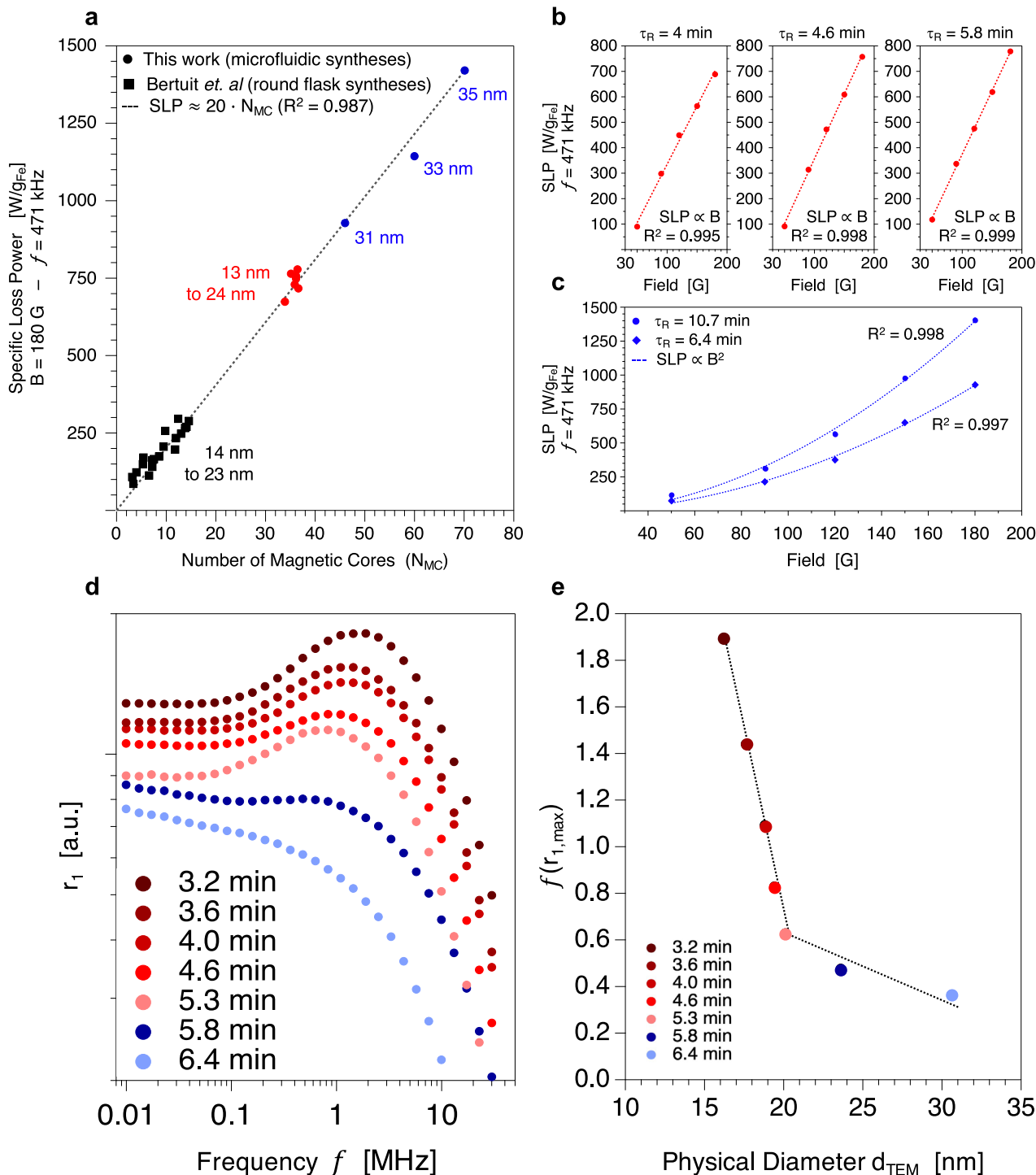


Fig. 3 NFs dynamic magnetic properties: magnetic hyperthermia and longitudinal relaxivity profiles. **a** SLP as a function of number of magnetic cores and comparison with previous work for an AMF of 180 G and 471 kHz. **b, c** SLP as a function of AMF strength at a fixed frequency of 471 kHz for residence times of 4, 4.6, 5.8 min and 6.4, 10.7 min. **d** r_1 longitudinal relaxivity profiles for different residence times. **e** Frequency position f of the maximum $r_{1,max}$ as a function of physical diameter.

correlation can be explained by an increase of the exchange couplings, that are an increasing function of N_{MC} in the case of flower-like nanoclusters²⁴. The same tendency was reported by Storozhuk *et al.*⁴⁹ who showed an increase in the SLP with the number of cores thanks to a seeded-growth synthesis enabling the obtention of nanoassemblies with various number of cores. Even if the number of cores was not determined in this study, the authors clearly show an increase in the SLP after the first and the second step of seeding associated to an increase in the number of cores evidenced by TEM

observations. In our case, high SLP ≥ 700 W/g values are reached, due to the high number of cores forming the nanossemblies obtained in the millifluidic device. NFs between 13 nm and 24 nm ($3 \text{ min} \leq \tau_R \leq 6 \text{ min}$, $N_{MC} = 35$) present intrinsic loss power (ILP) of $8.2 \pm 0.3 \text{ nH}\cdot\text{m}^2\cdot\text{kg}_{\text{Fe}}^{-1}$, which are higher than most of the previously reported values for iron oxide NFs of similar sizes. Hugouenq *et al.*²⁴ reported ILP up to $6.4 \text{ nH}\cdot\text{m}^2\cdot\text{kg}_{\text{Fe}}^{-1}$ for 24 nm NFs obtained by 48 h polyol synthesis. Herein, for residence times of 6.4 min (31 nm, $N_{MC} = 45$), 8 min (33 nm, $N_{MC} = 60$), and

10.7 min (35 nm, $N_{MC} = 70$), higher ILP values of 9.5, 11.7, and 14.5 $\text{nH}\cdot\text{m}^2\cdot\text{kg}_{\text{Fe}}^{-1}$ are reached. To the best of our knowledge, such ILP are higher than all previously reported values for iron oxide nanomaterials, even superior to the value of 8.1 $\text{nH}\cdot\text{m}^2\cdot\text{kg}_{\text{Fe}}^{-1}$ obtained very recently by Storozhuk et al.⁴⁹ for 32 nm multi-core clusters synthesized by a seeded-growth polyol strategy. The magnetothermal behavior of the as-synthesized NFs is also investigated under various AMF conditions, for a frequency of 471 kHz and variable B amplitudes from 50 to 180 G (Fig. 3b, c). For residence times of 4, 4.6, and 5.8 min ($13 \text{ nm} \leq d_{\text{TEM}} \leq 24 \text{ nm}$, $N_{MC} = 35$), SLP increases linearly with the AMF amplitude (B). A behavior change is evidenced at higher residence times of 6.4 min (31 nm, $N_{MC} = 45$) and 10.7 min (35 nm, $N_{MC} = 70$) for which SLP varies as the square of the AMF amplitude (B^2). Therefore, it suggests that the thermal losses subsequent to the AMF excitation are due to different relaxation processes, these being related to the magnetic properties' evolution during the NFs formation. For $\tau_R \leq 5.8 \text{ min}$ ($N_{MC} = 35$), the MHT efficiency is mostly caused by Néel relaxation while for $\tau_R \geq 6.4 \text{ min}$ ($N_{MC} \geq 45$) Brownian fluctuations become predominant. To support such hypothesis, $r_1(f)$ longitudinal NMR relaxivity profiles are measured. A strong evolution is observed depending on the residence times, going from the characteristic features for superparamagnetic nanoparticles (i.e., plateau at low frequency, broad peak around few MHz followed by drop of R_1 at high frequency) to those for Brown dominated particles (i.e., quasi plateau at low frequency followed by R_1 drop at high frequency)⁵⁰. Importantly, this evolution is not monotonous. Up to 5.3 min, few changes occur. The peak is clearly visible and its position $f(r_{1,\text{max}})$ is progressively slightly shifted to lower frequency (Fig. 3e). As shown in literature^{51,52}, $f(r_{1,\text{max}})$ shifts to lower frequency with the size of the particle, for a given polydispersity. From 5.8 min, the peak becomes suddenly barely visible and $f(r_{1,\text{max}})$ seems to weakly change. To shed light on the underlying processes ruling these NMR relaxivity profiles, their characteristic features should be detailed. They consist in three components named the well-known Curie term, the average fluctuation of the Curie term and the transversal contribution⁵⁰. The broad r_1 peak (Fig. 3d) originating from the second contribution is linked to the Néel relaxation^{53,54}. When the magnetic anisotropy increases, i.e., when the magnetic moment becomes blocked on the particles axis and the transversal contribution becomes predominant in the NMR ^1H relaxation processes masking this peak^{50,55}. Taken together, both MHT and NMR relaxometry results evidence the behavior modification in terms of magnetic spin relaxation, going from Néel-mode dominant NFs to Brownian-mode dominant NFs after $\tau_{\text{switch}} = 5.8 \text{ min}$.

The crucial role of nanoclusters mosaicity. In the case of molecular magnets, numerical simulations and experiments have shown that the magnetic coupling (E_{ij}) between two atom centers i and j is described by:

$$E_{ij} = -J_{ij} \cdot S_i \cdot S_j \cdot \cos(\theta_{ij}) \quad (1)$$

where J_{ij} is the coupling constant, S_i and S_j the magnetic spins of centers i and j , and θ_{ij} the angle between the two atom magnetic spins. As θ_{ij} regulates magnetic properties of molecular magnets, HR-TEM were performed to evaluate the misalignment of the different cores within a single NF. The angular dispersion, also called mosaicity, is a measure of the spread of the crystal plane orientations that can be obtained from the angular sprawl of diffraction peaks on the fast Fourier transform (FFT) of HR-TEM images for each residence time (Fig. 4a–h). In some cases, FFT are measured on four different areas inside the same nanoassembly (Fig. 4a, d, g). The four distinct FFT show very similar signatures and are superimposable with the global FFT of the whole

nanoassembly. Such an observation evidences the highly mono-crystalline character of the as-synthesized NFs. Strikingly, the evolution of mosaicity ($\Delta\theta$) with residence time follows a sigmoid decreasing function characterized by $\tau_{R,\text{half}} = 5.7 \text{ min}$ (Fig. 4i), close to all previously determined characteristic times associated to nanostructural, magnetic, and optical property switches. Based on these observations, we consequently draw the following mechanism: the clusters generated after the nucleation and attachment steps (Fig. 1f) are attached with $\Delta\theta_{\text{max}} = 6.5^\circ$ probably driven by an oriented auto-assembling process⁵⁶. During the subsequent growth stage (Fig. 1f), while each magnetic core grows by molecular diffusion, the crystalline cores continue progressively to align with each other. The oriented attachment continues also during the final aggregation stage (Fig. 1f), where the fusion of one NF to other leads to an angular defect of only $\Delta\theta_{\text{min}} = 3.5^\circ$.

According to molecular magnetism theory (Eq. 1), important θ_{ij} variations triggers major changes in the magnetic coupling: such an effect is observed in the case of NFs for which mosaicity variations are responsible for both M_S and ILP changes. Finally, both $1/E_U$ values and $R_1(\text{max})/R_1(0)$ values, characteristic of the Néel contribution in magnetic spin relaxation processes³¹, are plotted against mosaicity (Fig. 5a). Disorder effects at core boundaries should lead to changes in E_U values, as previously discussed. The linear increase in $1/E_U = f(\Delta\theta)$ also suggests that a crystal with a mosaicity of 2° should present an infinite E_U value, so that core boundaries defects become neglectable for $\Delta\theta \leq 2^\circ$. Moreover, the increase in Brownian spin relaxation with residence times evidenced by relaxometry measurements can be ascribed to the diminution of mosaicity. As the alignment of the cores goes from $\Delta\theta_{\text{max}} = 6.5^\circ$ to $\Delta\theta_{\text{min}} = 3.5^\circ$, the nanoassembly becomes more coherent and NFs tend to behave as one single big rigid magnetic dipole rather than a cluster composed of several cores⁵⁷. Concerning optical properties, a similar analogy can be established between molecular theories and NFs optical features. The excitonic theory for supramolecular assemblies predicts that the angle θ between electronic absorption momentum of aggregated molecules is the geometrical parameter that controls electronic transitions⁵⁸. In the case of molecular H-aggregates, which consist in a molecular π -stacking, electronic transitions become more and more symmetrically allowed when θ decreases from 180° (antiparallel configuration) to 0° (parallel configuration). Such phenomenon can be ascribed by the evolution of extinction coefficient values, signature of an electronic transition. In the case of NFs, a high increase in ϵ_{core} is observed when the mosaicity $\Delta\theta$ decreases (Fig. 5b). Assuming that the direction of core absorption momentum is conditioned by the crystallographic core orientations, the evolution of ϵ_{core} with $\Delta\theta$ reflects that the electronic transition around 1064 nm (IVCT) is more allowed when cores tend to reach a parallel configuration. As a result, we can conclude that flower-like nanoclusters obey to the excitonic theory for H-aggregates (Fig. 5c, d), where each core acts as a molecular brick whose orientation conditions the electronic transitions.

Conclusion. The correlation of NFs formation mechanism at the nanoscale with their magneto-optical properties and their fine high-resolved structures evidences the crucial role of mosaicity. This latter is found to regulate the static and dynamic magnetic properties of the molecular assemblies impacting their function by hyperthermia. Moreover, the nanoclusters can be described as a supramolecular optical aggregate where each core acts as a molecular brick whose orientation regulates the optical properties, as predicted by the molecular excitonic theory for H-aggregates. We believe that these results will have direct impact in the field materials science providing us with a new bottom-up concept based on manipulation of mosaicity by chemical

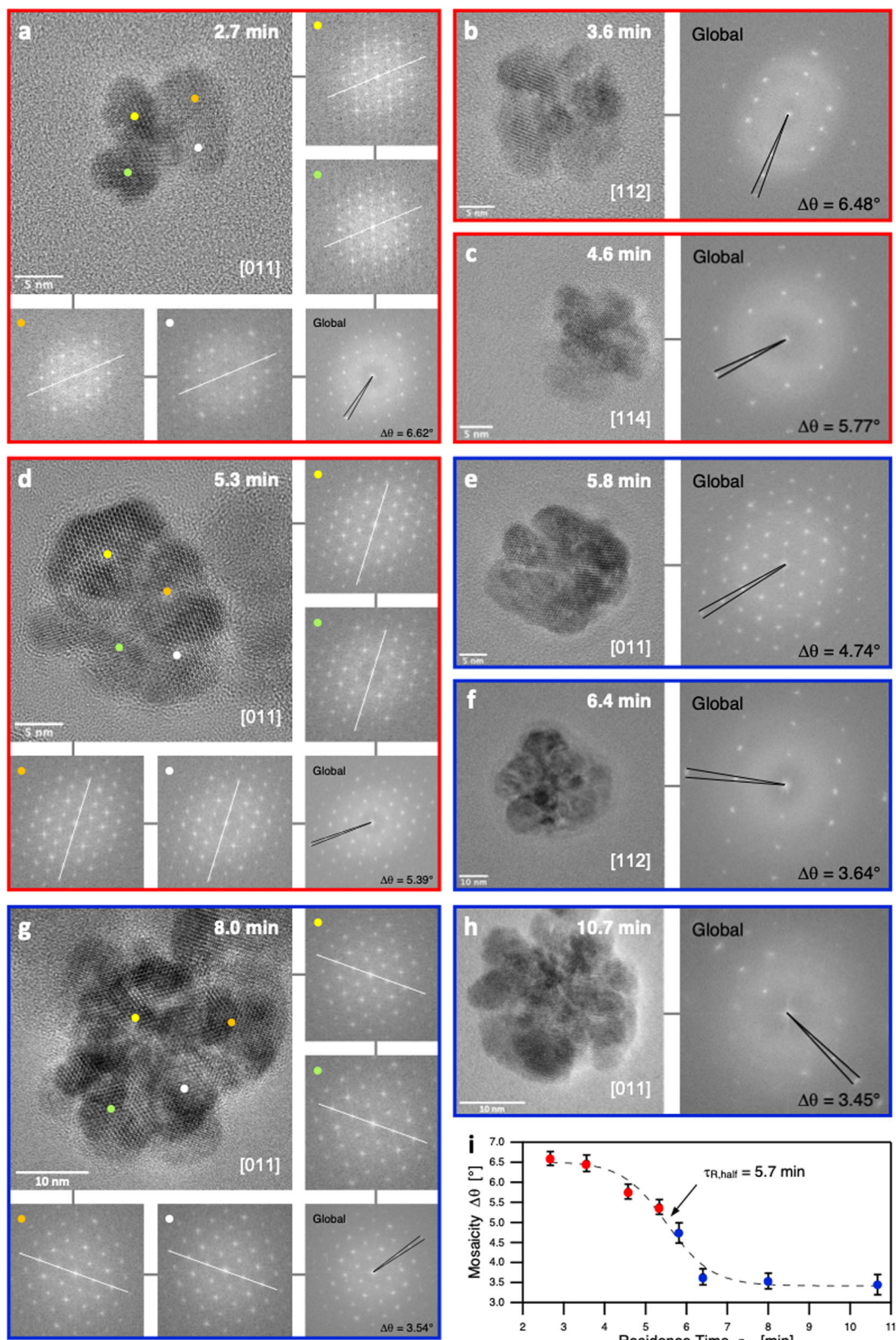


Fig. 4 Fine-structure analysis of core disorders. **a-h** HR-TEM micrographs of the NFs and their corresponding FFT for mosaicity measurements ($\Delta\theta$) during growth (red: **a, b, c, d**) and aggregation (blue: **e, f, g, h**) stages. **i** Mosaicity as a function of residence time. Error bars correspond to the standard deviation obtained from the measurements of mosaicity on 15 different isolated NFs for each residence times. White solid lines: eye-guide for an easier comparison of the local FFT; black solid lines: angular measurements of the mosaicity values.

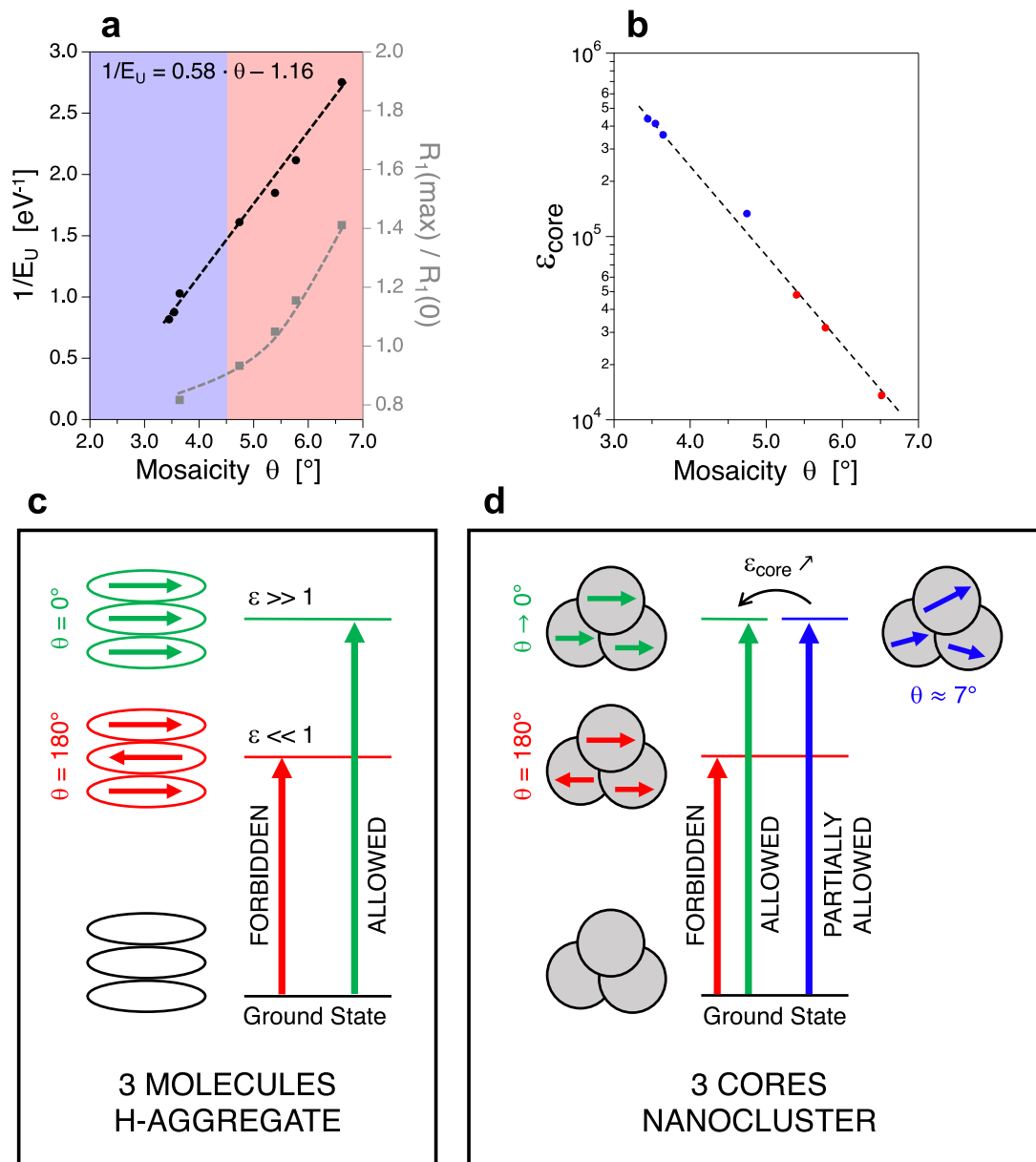


Fig. 5 Impact of mosaicity on the optical properties. **a** Defect-characteristic $1/E_U$ values (black circles) and Néel contribution ($R_1(\text{max})/R_1(0)$, gray squares) as a function of mosaicity. **b** Evolution of the extinction coefficient of one core ($\epsilon_{\text{core}} = \epsilon_{\text{NP}}/N_{\text{MC}}$) at 1064 nm with mosaicity. **c** Description of the optical theory for excitonic absorption in molecular H-aggregates. **d** Analogy of the molecular excitonic theory in the case of multi-core nanoclusters such as NFs.

synthesis conditions in order to program their individual or collective properties for optimized functions.

Experimental section

Materials. N-methyldiethanolamine (NMDEA, >99%), diethylene glycol (DEG, >99%), iron(III) chloride hexahydrate ($\text{FeCl}_3 \cdot 6\text{H}_2\text{O}$, 99%), iron(II) chloride tetrahydrate ($\text{FeCl}_2 \cdot 4\text{H}_2\text{O}$, 99%) are purchased from Merck (Darmstadt, Germany). Sodium hydroxide pellets (NaOH, 99%), hydrochloric acid (HCl, 37%), ethanol (96%), nitric acid (HNO_3 , 68%), acetone (>99%), and diethyl ether (Et_2O , 100%) are purchased from VWR International (Rosny-sous-Bois, France). All chemicals are used without further purification. Analytical HPLC pump ECP2000 is purchased from ECOM (Prague, Czech Republic).

Millifluidic flow system. Stainless steel millifluidic channels (inner diameter: 0.040", outer diameter: 1/16") are purchased from Cluzeau Info Lab (Sainte-Foy-la-Grande, France). Proportional-integral-differential (PID) controllers (77 mm \times 35 mm, 220 V, -200 to 600 °C), Pt100 temperature probes, heating cartridges (16 mm \times 200 mm, 1 kW, 220 V), electrical fuses (16A and 64A), on/off switching buttons and electrical cables (1.3 mm² and 2.1 mm²) are from Radio Spare Pro™ (Beauvais, France).

Flow synthesis procedure. All the iron oxide NFs presented in this work are synthesized using a previously described millifluidic system by a modified polyol route³². The flow system is filled with DEG using a flow rate of 5 mL·min⁻¹ during 4 min. The PID control boxes are then set to a temperature of 220 °C and the flow rate is decreased to 1 mL·min⁻¹. Once the thermal equilibrium is reached (about 5 min), the reactive media is used as the inlet

solution and is injected at the desired flow rate. After a time of $t = 1.5 \tau_R$, the collecting flask is replaced by a new one to collect only the products of the reaction (without collecting the initial DEG or eventual impurities). Once a sufficient volume of crude product is obtained, the collecting flask is replaced by another one. The PID control boxes are set to 20 °C and a DEG flow of 2 mL·min⁻¹ is injected to clean the inside of the millifluidic channel while the temperature decreases. Once the system reaches ambient temperature, 200 mL of water are injected at a high flow rate of 10 mL·min⁻¹ to remove any remaining impurities. Finally, the HPLC pump, each PID control box and the general electrical control box are switched off.

Ex situ kinetic studies. At the end of the millifluidic device, the crude product is collected in a flask which is placed in a cooling bath in order to quench the reaction yielding to the formation of NFs. The crude product is then washed and characterized by several methods. With such a process, ex situ kinetic studies are both easy and relevant as the reaction is stopped at the outlet of the system.

NFs characterization. The total iron concentrations of NFs suspensions are measured by atomic absorption spectroscopy (AAS, PinAAcle 500, Perkin Elmer) degrading the samples in concentrated HCl (37%) before a dilution in HNO₃ (2%). NFs are imaged using a JEOL-1011 transmission electron microscope operating at 100 kV. Size distributions are determined thanks to Image J software by measuring manually 300 NFs on at least three different images. The resulting histograms are modeled by log-normal laws using Igor Pro 7 software to determine the mean physical diameter and the polydispersity of each sample. High-resolution TEM is performed on a JEOL 2010 operating at 200 kV. Magnetization curves (for Langevin models) are measured using a home-made vibrating sample magnetometer in the range 0–800 kA/m. Magnetization hysteresis loops (for M_S determination) are measured on a MPMS-XL7 Quantum Design SQUID in the range –20 kOe to 20 kOe.

Determination of the number of magnetic cores per nanoassembly. The size of each magnetic core (d_m) are determined thanks to $M = f(H)$ curves modeled by a log-normal weighted Langevin law. As the physical diameter (d_{TEM}) of the whole nanoassembly is known (by TEM measurements), assuming that both magnetic cores and nanoassemblies are spherical, one can obtain the number of magnetic cores (N_{MC}) per nanoassembly: $N_{MC} = (d_{TEM}/d_m)^3$.

Magnetic hyperthermia. The experiments are carried out in 0.5 mL Eppendorf® containing 50 µL of the NPs suspensions excited for 600 s by an alternating magnetic field generator device (DM3, NanoScale Biomagnetics) operating at a frequency of 471 kHz with amplitudes ranging from 50 G to 180 G. Temperature increase are measured by an infrared camera FLIR SC7000.

NMR relaxometry. The measurements of the water ¹H longitudinal relaxation rates $R_1 = 1/T_1$ (and the related relaxivity $r_1 = R_1/[Fe]$) have been carried out using Stellar SpinMaster relaxometer, in the 10 kHz to 30 MHz frequency range (¹H frequency). A pre-polarized sequence has been used from 10 kHz to 10 MHz and a non-polarized sequence from 10 MHz to 30 MHz⁵⁹. The samples put in glass tubes 10 mm external in diameter and 40 mm in length closed by a silicon cap, were thermostated at 298 K using regulated air flux.

X-ray scattering and absorption. Small angle X-ray scattering is performed at Synchrotron SOLEIL on the SWING line in 1 mm

diameter glass capillary. X-ray absorption near edge spectroscopy at Fe K-edge is performed at Synchrotron SOLEIL on the ROCK line in 1 mm diameter glass capillary, using a Si(111) monochromator.

Optical characterization. UV-Vis-NIR spectra (400–1100 nm) are recorded at room temperature in a 1 cm quartz cuvette using an Avantes spectrophotometric set-up composed of an AvaLight-DHc lamp connected by optical fibers to a StarLine AvaSpec UV/Vis detector and to a NIRLine AvaSpec-NIR256-1.7 NIR detector.

Data availability

A Supplementary Information file is available together with this manuscript. It includes a global description of the millifluidic system, TEM of figures corresponding to the different residence times, size distribution histograms analysis, magnetization curves, SAXS analysis, magnetization curves, XANES analysis, UV-Vis-NIR absorption spectra, Beer Lambert plots, Tauc plots, Urbach plots and temperature elevation curves obtained in MHT. The data that support the findings of this study are available from the corresponding author A.A.-H.

Received: 24 August 2022; Accepted: 24 November 2022;

Published online: 02 December 2022

References

- Hao, R. et al. Synthesis, functionalization, and biomedical applications of multifunctional magnetic nanoparticles. *Adv. Mater.* **22**, 2729–2742 (2010).
- Shasha, C. & Krishnan, K. M. Nonequilibrium dynamics of magnetic nanoparticles with applications in biomedicine. *Adv. Mater.* **33**, 1904131 (2021).
- Rigoni, C. et al. Division of ferrofluid drops induced by a magnetic field. *Langmuir* **34**, 9762–9767 (2018).
- Rigoni, C. et al. Dynamics of ferrofluid drops on magnetically patterned surfaces. *Langmuir* **34**, 8917–8922 (2018).
- Lim, E.-K. et al. pH-Triggered drug-releasing magnetic nanoparticles for cancer therapy guided by molecular imaging by MRI. *Adv. Mater.* **23**, 2436–2442 (2011).
- Gloag, L., Mehdipour, M., Chen, D., Tilley, R. D. & Gooding, J. J. Advances in the application of magnetic nanoparticles for sensing. *Adv. Mater.* **31**, 1904385 (2019).
- Derfus, A. M. et al. Remotely triggered release from magnetic nanoparticles. *Adv. Mater.* **19**, 3932–3936 (2007).
- Balakrishnan, P. B. et al. Exploiting unique alignment of cobalt ferrite nanoparticles, mild hyperthermia, and controlled intrinsic cobalt toxicity for cancer therapy. *Adv. Mater.* **32**, 2003712 (2020).
- Espinosa, A. et al. Magnetic (hyper)thermia or photothermia? Progressive comparison of iron oxide and gold nanoparticles heating in water, in cells, and in vivo. *Adv. Funct. Mater.* **28**, 1803660 (2018).
- Bertuit, E. et al. Structure–property–function relationships of iron oxide multicore nanoflowers in magnetic hyperthermia and photothermia. *ACS Nano* **16**, 271–284 (2022).
- Nemes, S. et al. Comparison of iron oxide nanoparticles in photothermia and magnetic hyperthermia: effects of clustering and silica encapsulation on nanoparticles' heating yield. *Appl. Sci.* **10**, 7322 (2020).
- Li, W. et al. Colloidal molecules and patchy particles: complementary concepts, synthesis and self-assembly. *Chem. Soc. Rev.* **49**, 1955–1976 (2020).
- van Blaaderen, A. Colloids get complex. *Nature* **439**, 545–546 (2006).
- Blaaderen, A. V. CHEMISTRY: colloidal molecules and beyond. *Science* **301**, 470–471 (2003).
- Penn, R. L. & Banfield, J. F. Imperfect oriented attachment: dislocation generation in defect-free nanocrystals. *Science* **281**, 969–971 (1998).
- Yoreo, J. J. D. et al. Crystallization by particle attachment in synthetic, biogenic, and geologic environments. *Science* **349**, aaa6760 (2015).
- Jehannin, M., Rao, A. & Cölfen, H. New horizons of nonclassical crystallization. *J. Am. Chem. Soc.* **141**, 10120–10136 (2019).
- Lee, J., Yang, J., Kwon, S. G. & Hyeon, T. Nonclassical nucleation and growth of inorganic nanoparticles. *Nat. Rev. Mater.* **1**, 16034 (2016).
- Wang, S. et al. The emergence of valency in colloidal crystals through electron equivalents. *Nat. Mater.* **21**, 580–587 (2022).
- Liu, L. et al. Connecting energetics to dynamics in particle growth by oriented attachment using real-time observations. *Nat. Commun.* **11**, 1045 (2020).
- Mirabella, G. et al. Crystallization by particle attachment is a colloidal assembly process. *Nat. Mater.* **19**, 391–396 (2020).
- Wang, Y. et al. The predominant role of collagen in the nucleation, growth, structure and orientation of bone apatite. *Nat. Mater.* **11**, 724–733 (2012).

23. Gavilán, H. et al. Formation mechanism of maghemite nanoflowers synthesized by a polyol-mediated process. *ACS Omega* **2**, 7172–7184 (2017).
24. Hugouenq, P. et al. Iron oxide monocrystalline nanoflowers for highly efficient magnetic hyperthermia. *J. Phys. Chem. C* **116**, 15702–15712 (2012).
25. Hemery, G. et al. Tuning sizes, morphologies, and magnetic properties of monocoresh versus multicore iron oxide nanoparticles through the controlled addition of water in the polyol synthesis. *Inorg. Chem.* **56**, 8232–8243 (2017).
26. Cabana, S., Curcio, A., Michel, A., Wilhelm, C. & Abou-Hassan, A. Iron oxide mediated photothermal therapy in the second biological window: a comparative study between magnetite/maghemite nanospheres and nanoflowers. *Nanomaterials* **10**, 1548 (2020).
27. Lartigue, L. et al. Cooperative organization in iron oxide multi-core nanoparticles potentiates their efficiency as heating mediators and MRI contrast agents. *ACS Nano* **6**, 10935–10949 (2012).
28. Gallo-Cordova, A. et al. Unravelling an amine-regulated crystallization crossover to prove single/multicore effects on the biomedical and environmental catalytic activity of magnetic iron oxide colloids. *J. Colloid Interface Sci.* **608**, 1585–1597 (2022).
29. Mirabello, G. et al. Understanding the formation mechanism of magnetic mesocrystals with (cryo-)electron microscopy. *Chem. Mater.* **31**, 7320–7328 (2019).
30. Verdaguer, M. Rational synthesis of molecular magnetic materials: a tribute to Olivier Kahn. *Polyhedron* **20**, 1115–1128 (2001).
31. Hestand, N. J. & Spano, F. C. Expanded theory of H- and J-molecular aggregates: the effects of vibronic coupling and intermolecular charge transfer. *Chem. Rev.* **118**, 7069–7163 (2018).
32. Bertuit, E., Neveu, S. & Abou-Hassan, A. High temperature continuous flow syntheses of iron oxide nanoflowers using the polyol route in a multi-parametric millifluidic device. *Nanomaterials* **12**, 119 (2022).
33. Gavilán, H. et al. Magnetic nanoparticles and clusters for magnetic hyperthermia: optimizing their heat performance and developing combinatorial therapies to tackle cancer. *Chem. Soc. Rev.* **50**, 11614–11667 (2021).
34. Zeng, H., Li, J., Liu, J. P., Wang, Z. L. & Sun, S. Exchange-coupled nanocomposite magnets by nanoparticle self-assembly. *Nature* **420**, 395–398 (2002).
35. O’Handley, R. C. *Modern Magnetic Materials: Principles and Applications* (Wiley, 2000).
36. Donaldson, J. G., Schall, P. & Rossi, L. Magnetic coupling in colloidal clusters for hierarchical self-assembly. *ACS Nano* **15**, 4989–4999 (2021).
37. Petit, P.-E., Farges, F., Wilke, M. & Sole, V. A. Determination of the iron oxidation state in Earth materials using XANES pre-edge information. *J. Synchrotron Radiat.* **8**, 952–954 (2001).
38. Kuzmin, A. & Chaboy, J. EXAFS and XANES analysis of oxides at the nanoscale. *IUCr* **1**, 571–589 (2014).
39. Wilke, M., Farges, F., Petit, P.-E., Brown, G. E. & Martin, F. Oxidation state and coordination of Fe in minerals: an Fe K-XANES spectroscopic study. *Am. Mineralogist* **86**, 714–730 (2001).
40. Tang, J., Myers, M., Bosnick, K. A. & Brus, L. E. Magnetite Fe₃O₄ nanocrystals: spectroscopic observation of aqueous oxidation kinetics. *J. Phys. Chem. B* **107**, 7501–7506 (2003).
41. Wasim, S. et al. Effect of structural disorder on the Urbach energy in Cu ternaries. *Phys. Rev. B* **64**, 195101 (2001).
42. Hassanien, A. S. & Akl, A. A. Effect of Se addition on optical and electrical properties of chalcogenide CdSSe thin films. *Superlattices Microstructures* **89**, 153–169 (2016).
43. Fontijn, W. F. J., vanderZaag, P. J., Devillers, M. A. C., Brabers, V. A. M. & Metselaer, R. Optical and magneto-optical polar Kerr spectra of Fe₃O₄ and Mg²⁺- or Al³⁺-substituted Fe₃O₄. *Phys. Rev. B* **56**, 5432–5442 (1997).
44. Akshay, V. R., Arun, B., Mandal, G. & Vasundhara, M. Visible range optical absorption, Urbach energy estimation and paramagnetic response in Cr-doped TiO₂ nanocrystals derived by a sol-gel method. *Phys. Chem. Chem. Phys.* **21**, 12991–13004 (2019).
45. Niculaes, D. et al. Asymmetric assembling of iron oxide nanocubes for improving magnetic hyperthermia performance. *ACS Nano* **11**, 12121–12133 (2017).
46. Lak, A. et al. Fe²⁺ deficiencies, FeO subdomains, and structural defects favor magnetic hyperthermia performance of iron oxide nanocubes into intracellular environment. *Nano Lett.* **18**, 6856–6866 (2018).
47. Orozco-Henao, J. M., Muraca, D., Sánchez, F. H. & Mendoza Zélis, P. Palmitic acid-coated magnetite nanocubes with high-quality crystallinity and bulk-like magnetic features. *J. Phys. D: Appl. Phys.* **53**, 385001 (2020).
48. Atkinson, W. J., Brezovich, I. A. & Chakraborty, D. P. Usable frequencies in hyperthermia with thermal seeds. *IEEE Trans. Biomed. Eng.* **BME-31**, 70–75 (1984).
49. Storozhuk, L. et al. Stable iron oxide nanoflowers with exceptional magnetic heating efficiency: simple and fast polyol synthesis. *ACS Appl. Mater. Interfaces* **13**, 45870–45880 (2021).
50. Rollet, A.-L. et al. New approach for understanding experimental NMR relaxivity properties of magnetic nanoparticles: focus on cobalt ferrite. *Phys. Chem. Chem. Phys.* **18**, 32981–32991 (2016).
51. Vuong, Q. L., Berret, J. F., Fresnais, J., Gossuin, Y. & Sandre, O. A universal scaling law to predict the efficiency of magnetic nanoparticles as MRI T(2)-contrast agents. *Adv. Health. Mater.* **1**, 502–512 (2012).
52. Fresnais, J. et al. NMR relaxivity of coated and non-coated size-sorted maghemite nanoparticles. *Mol. Phys.* **117**, 990–999 (2019).
53. Roch, A., Muller, R. N. & Gillis, P. Theory of proton relaxation induced by superparamagnetic particles. *J. Chem. Phys.* **110**, 5403–5411 (1999).
54. Gossuin, Y., Gillis, P., Hocq, A., Vuong, Q. L. & Roch, A. Magnetic resonance relaxation properties of superparamagnetic particles. *WIREs Nanomed. Nanobiotechnology* **1**, 299–310 (2009).
55. Lévy, M. et al. Revisiting MRI contrast properties of nanoparticles: beyond the superparamagnetic regime. *J. Phys. Chem. C* **117**, 15369–15374 (2013).
56. Lin, M., Tan, H. R., Tan, J. P. Y. & Bai, S. Understanding the growth mechanism of α -Fe₂O₃ nanoparticles through a controlled shape transformation. *J. Phys. Chem. C* **117**, 11242–11250 (2013).
57. Bender, P., Honecker, D. & Barquin, L. F. Superferromagnetic correlations in clusters of magnetic nanoflowers. *Appl. Phys. Lett.* **115**, 132406 (2019).
58. Ma, S. et al. Organic molecular aggregates: from aggregation structure to emission property. *Aggregate* **2**, e96 (2021).
59. Anordo, E., Galli, G. & Ferrante, G. Fast-field-cycling NMR: Applications and instrumentation. *Appl. Magn. Reson.* **20**, 365–404 (2001).

Acknowledgements

E.B. and A.A.-H. acknowledge French Doctoral School ED388. This work was also supported by the Agence Nationale de la Recherche (ANR) through the ANR-18-849-CE09-0004 (MicroNanoCell project). The authors acknowledge the staff of the MPBT (physical properties—low temperature) platform of Sorbonne Université for their support. We acknowledge SOLEIL for provision of synchrotron radiation facilities (SAXS, XAS) and we would like to thank Valérie Briois for assistance in using beamline ROCK: these measurements were supported by a public grant overseen by the French National Research Agency (ANR) as part of the “Investissements d’Avenir” program (reference: ANR-10-EQPX-45). The authors also thank Aude Michel-Tourgis, and Delphine Talbot (PHENIX, Sorbonne Université) for iron concentration measurements by AAS.

Author contributions

E.B. and A.A.-H. conceived and designed the experiments, E.B., N.M., and A.-L.R. performed the experiments; E.B. analyzed data; E.B., N.M., C.W., A.-L.R., and A.A.-H. interpreted data; E.B. and A.A.-H. wrote the paper.

Competing interests

The authors declare no competing interests.

Additional information

Supplementary information The online version contains supplementary material available at <https://doi.org/10.1038/s42004-022-00787-0>.

Correspondence and requests for materials should be addressed to Ali Abou-Hassan.

Peer review information *Communications Chemistry* thanks the anonymous reviewers for their contribution to the peer review of this work.

Reprints and permission information is available at <http://www.nature.com/reprints>

Publisher’s note Springer Nature remains neutral with regard to jurisdictional claims in published maps and institutional affiliations.



Open Access This article is licensed under a Creative Commons Attribution 4.0 International License, which permits use, sharing, adaptation, distribution and reproduction in any medium or format, as long as you give appropriate credit to the original author(s) and the source, provide a link to the Creative Commons license, and indicate if changes were made. The images or other third party material in this article are included in the article’s Creative Commons license, unless indicated otherwise in a credit line to the material. If material is not included in the article’s Creative Commons license and your intended use is not permitted by statutory regulation or exceeds the permitted use, you will need to obtain permission directly from the copyright holder. To view a copy of this license, visit <http://creativecommons.org/licenses/by/4.0/>.

© The Author(s) 2022